



Multiphysics modeling of carbon gasification processes in a well-stirred reactor with detailed gas-phase chemistry

Li Qiao ^{a,*}, Jian Xu ^a, Anup Sane ^b, Jay Gore ^b

^aSchool of Aeronautics and Astronautics, Purdue University, West Lafayette, IN 47907, United States

^bSchool of Mechanical Engineering, Purdue University, West Lafayette, IN 47907, United States

ARTICLE INFO

Article history:

Received 5 April 2011

Received in revised form 17 August 2011

Accepted 3 December 2011

Available online 7 January 2012

Keywords:

Coal gasification

Carbon gasification

Detailed chemistry

Heterogeneous surface reactions

Radiation

Multi-physics numerical modeling

ABSTRACT

Fuel synthesis through coal and biomass gasification has the potential to provide a solution to the increasing demand for energy and transportation fuels. To theoretically understand the complex chemical processes in a gasifier and to identify the most influential parameters for syngas production, we developed a multiphysics model to simulate the gasification processes in a well-stirred reactor. This model is the first of its kind and considers detailed gas-phase chemistry, particle-phase reactions, radiative heat transfer, as well as full coupling between the two phases at various scales for mass, species, and energy exchange. The gas-phase reactions use the detailed chemistry GRI-Mech 1.2, including 177 elementary reactions and 31 species, as well as variable thermodynamic and transport properties. Four surface reactions were considered and the reaction rates were simulated by the diffusion-kinetics model with consideration of boundary layer diffusion. A random pore model was used to account for the evolution of the char porous structure and its impact on gasification rates. A numerical code was developed to solve the gas-phase and the particle-phase governing equations. Numerical simulations were conducted to understand the gasification process and the effects of particle size, porous structure, radiative heat transfer, pressure, O₂ concentration, and H₂ addition on gasification performance.

© 2011 The Combustion Institute. Published by Elsevier Inc. All rights reserved.

1. Introduction

Fuel synthesis through coal gasification offers a potential solution to the problem of increasing demand for energy and transportation fuels. The understanding of the complex chemical processes in coal gasification through experimental and computational means has generated increasing interest over recent years. In terms of modeling coal gasification processes, previous works have focused mainly on three areas: single coal particle gasification [1–3], one-dimensional coal gasification [4–7], and computational fluid dynamics (CFD) of coal gasification reactors [8–12]. CFD modeling of entrained flow reactors is extremely complex, involving gas-phase turbulent flow and particle-phase turbulent flow, as well as particle-gas-phase coupling, which is beyond the scope of the present study and thus will not be discussed here.

The modeling of a single char particle offers a fundamental understanding of the gasification process. Srinivas and Amundson [1] developed a simple model for gasification of a single char particle. It solves the particle's mass and energy conservation equations with the Stefan-Maxwell relations assuming constant

transport and thermodynamic properties. Haynes [2] proposed an improved model that calculated diffusivities for different components. His model also has the capability to incorporate multiple reactions and components. Samoilov et al. [3] developed a model that emphasizes the effects of a porous structure of the char and surface reaction kinetics for a single carbon particle in a CO₂ environment. It used the Langmuir-Hinshelwood description of the porous structure, the diffusion processes, and the gasification processes. All these models, however, did not consider detailed devolatilization kinetics or char-surface reactions. Moreover, interactions between particles and between gas phase and particle phase were modeled in a simple way.

Govind and Shah [4] developed a 1-D mathematical model to simulate the Texaco downflow entrained bed gasifier that used coal-water slurries as the feedstock. The unreacted-core shrinking model was used to estimate the solid-gas reaction rates. Three crucial parameters, the coal-feeding rate, the oxygen to coal ratio, and the steam to coal ratio, were investigated, and their effects on the exhaust gas composition for the gasifier and the final carbon conversion were determined. Ni and Williams [5] developed a multi-variable model for an entrained flow coal-oxygen gasifier, which considered one-step devolatilization kinetics and one char surface reaction and assumed the gas-phase reactions to be at equilibrium. The effects of coal-oxygen-steam ratios, temperature, and pressure

* Corresponding author. Address: School of Aeronautics and Astronautics, Purdue University, 701 W. Stadium Ave., West Lafayette, IN 47907, United States.

E-mail address: lqiao@purdue.edu (L. Qiao).

Nomenclature

A_p	particle surface area (cm^2)	r_p	particle radius (cm)
B	transfer number	Sc	Sherwood number
B_i	Biot number	Q_h	enthalpy transferred from a particle to the bulk gases as a result of mass transfer because of surface reactions ($\text{erg cm}^{-3} \text{s}^{-1}$)
B_k	prefactor for surface reaction rate ($\text{g s}^{-1} \text{cm}^{-2} \text{atm}^{-1}$)	Sh	Sherwood number
$\bar{C}_{p,g}$	mean specific heat capacity of mixture ($\text{erg g}^{-1} \text{K}^{-1}$)	T	temperature (K)
$C_{p,p}$	specific heat capacity of carbon particle ($\text{erg g}^{-1} \text{K}^{-1}$)	t	time (s)
C_s	total gas concentration at the film at particle surface temperature (mol cm^{-3})	\overline{W}	mean molecular weight of mixture (g mol^{-1})
D	diffusivity ($\text{cm}^2 \text{s}^{-1}$)	W_C	molecular weight of carbon (g mol^{-1})
D_{im}	molecular diffusivity at the film temperature ($\text{cm}^2 \text{s}^{-1}$)	W_i	molecular weight of species i (g mol^{-1})
d_p	particle diameter (cm)	w_i	production rate of species i because of heterogeneous surface reactions ($\text{mol cm}^{-3} \text{s}^{-1}$)
E_k	activation energy (erg mol^{-1})	$X_{i,s}$	mole fraction of the species i at particle surface
e	internal energy of the bulk gases (erg g^{-1})	$X_{i,\infty}$	mole fraction of the species i in bulk gases
f_{RPM}	factor accounts for the pore surface evolution because of carbon conversion	x	carbon conversion ratio
h	convective heat transfer coefficient ($\text{erg s}^{-1} \text{cm}^{-2} \text{K}^{-1}$)	Y_i	mass fraction of species i in the gas mixture
h_i	specific enthalpy of species i (erg g^{-1})	Z	transfer number
K_g	thermal conductivity of gas mixture ($\text{erg s}^{-1} \text{cm}^{-1} \text{K}^{-1}$)		
K_{im}	mass transfer coefficient ($\text{mol s}^{-1} \text{cm}^{-2}$)		
K_k	surface reaction rate constant ($\text{g s}^{-1} \text{cm}^{-2} \text{atm}^{-1/n}$)		
K_p	thermal conductivity of the particle ($\text{erg s}^{-1} \text{cm}^{-1} \text{K}^{-1}$)		
m	mass (g)		
\dot{m}_C	surface reaction rate of reaction j (g s^{-1})		
N_p	particle number density (cm^{-3})		
N_u	Nusselt number		
$\dot{n}_{C,k}$	carbon molar reaction rate per unit area ($\text{mol s}^{-1} \text{cm}^{-2}$)		
\dot{n}_i	species molar flux of species i ($\text{mol s}^{-1} \text{cm}^{-2}$)		
P	pressure (atm)		
Q_c	heat of surface reaction ($\text{erg cm}^{-3} \text{s}^{-1}$)		
Q_{con}	convective heat transfer between a particle and the bulk gases ($\text{erg cm}^{-3} \text{s}^{-1}$)		
$Q_{p,rad}$	radiative heat transfer between a particle and the wall ($\text{erg cm}^{-3} \text{s}^{-1}$)		
$R_{C,i}$	species i generation rate resulting from surface reactions (g s^{-1})		
Re	Reynolds number		
R	gas constant ($\text{erg mol}^{-1} \text{K}^{-1}$)		

on gasification products and steam production were estimated. Later, Vamvuka and Woodburn [6] developed a 1-D steady-state entrained flow reactor model, which is based on mass and energy conservation equations, including solid-phase reactions and assuming gas-phase reactions at equilibrium. The temperature, reaction rate, and composition profiles were calculated to determine the effects of different operating parameters on gasifier performance. These models, however, considered rather simple heterogeneous surface reactions, neglecting detailed devolatilization kinetics and also the effects of a porous char structure on the diffusion process. Moreover, for gas-phase reactions only a few (up to 4) reactions were considered with a one-step overall reaction rate, and some reactions were assumed to be in equilibrium.

A more detailed 1-D plug-flow reactor model was developed by Liu et al. [7] for a pressurized entrained flow gasifier, which emphasized the influence of high pressure, reaction kinetics, and char structure on gasification performance. The sensitivity analyses show that reaction kinetics and char structure are both crucial for predicting coal gasification processes. Also, low-pressure gasification kinetics (i.e., pressure order) cannot be extrapolated to high-pressure conditions. Recently, Sane et al. [13] developed a multiphase well-stirred reactor model to simulate coal gasification. The model considers boundary layer gas diffusion reactions, two particle-phase surface reactions, and water-gas-shift reaction

in equilibrium in the gas phase. The results showed the effects of pressure, temperature, particle size, H₂O/coal ratio, and external H₂ addition on the carbon conversion and CO₂ emission rates.

In summary, previous studies have shown that several factors, including the detailed devolatilization kinetics, gas-phase reactions, char structure (through diffusion process), and char-surface reactions, can all influence the gasification process, especially at high pressures. The models in literature have mostly used simple gas-phase kinetics or reactions, and some reactions were assumed to be at equilibrium. The reaction rate has been mostly expressed in terms of a one-step overall reaction rate, which may not be sufficiently accurate for broader operating conditions. Furthermore, multiphysics interactions between gas phase and particle phase were not thoroughly considered in these models. Some interactions that account for the mass and energy exchange between the two phases were even neglected. These studies indicate that a more detailed model is needed, one that includes reaction diffusion processes, char structure, surface reactions, and interactions between the two phases at the boundary. Lastly, gas-phase homogeneous reactions and transport, which have an important impact on the gasification behavior, should be better described by the use of detailed chemistry, variable thermodynamic properties, and various multi-phase transport properties.

Motivated by this, we developed the present multiphysics model with detailed gas-phase chemistry and a numerical code

to simulate the complex carbon gasification processes in a perfectly stirred reactor. The model includes gas-phase and particle-phase reactions as well as a coupling that includes mass, species, and energy exchanges between the two phases at various scales. The gas-phase reactions used the detailed chemistry GRI-Mech 1.2 [14], including 177 elementary reactions and 31 species, and various transport properties and variable thermodynamic properties in CHEMKIN format. For the particle-phase, four surface reactions were considered. The surface reaction rates were simulated by using the diffusion-kinetics model with consideration of boundary layer mass and energy diffusion. Numerical simulations and parametric studies were conducted to understand the gasification process at various operating conditions. While we recognize that multiple choices exist for the selection of various reaction mechanisms, chemical and physical properties, and phase diagrams, representative results allowing conclusions that are qualitatively independent and quantitatively change only insignificantly, with specific model selection, are presented.

2. Model description

Figure 1 shows a schematic of a well-stirred reactor for which the multiphysics model with detailed chemistry described in the previous section was developed to simulate carbon gasification processes. Although the depiction in Fig. 1 is spherical, the well stirred reactor can be of any well defined geometric shape. Carbon particles with diameter d_p are uniformly distributed inside the reactor together with gaseous species. The reactor's pressure remains constant, which means that during the gasification process the volume increases as a result of thermal expansion; thus the number density of coal particles decreases, but the total number is conserved. It is assumed that intense mixing occurs inside the reactor so that all gas-phase properties in the gas-phase bulk of the reactor, with the exception of the small boundary layers surrounding the particles, are uniform or spatially independent. As a result of this assumption, the temperature and number density of the particles can be assumed to be uniform at the bulk scale of the reactor. Mass, species, and energy exchanges between individual particles and surrounding gases cause local nonequilibrium in the boundary layers surrounding each of the particles. These interactions are modeled on the particle scale. Moreover, the model developed for a single particle represents all particles inside the reactor. For the gas-phase reactions, detailed kinetics and variable thermodynamic properties are considered. The governing equations of mass, species, and energy conservation for the gas phase and the particle phase are coupled to account for mass, species, and energy exchanges between the two phases. The transient gasification process is computed until 99% of the coal particle is gasified. Additional assumptions that are of immediate convenience but do not impact the conclusions of the present study include uniformity of temperature within the particle phase as a

result of the small size and large thermal conductivity of particles and spherically symmetric gradient diffusion heat and mass transfer to the particle surface from the bulk gas phase. In particular, the Biot number was found to be very small ($\sim 10^{-4}$) for the present simulations. Note the Biot number is defined as $Bi = hd_p/k_p$, where h is the convective heat transfer coefficient, and k_p is the thermal conductivity of the particle. The small Biot number implies that heat conduction inside the particle is much faster than the heat convection away from its surface, and thus temperature gradients are negligible inside of the particle. Equal binary diffusion coefficients are considered applicable for multi-species diffusion and the bulk gas properties are modeled using ideal gas law. The governing equations in the Eulerian coordinate system for the gas and particle phases resulting from the above assumptions are described in the following section.

2.1. Gas-phase equations

The conservation equations of mass, species, and energy for the gas phase are

$$\frac{dm_g}{dt} = \frac{m_g}{\rho_g} \sum w_i W_i \quad (1.1)$$

$$\rho_g \frac{dY_i}{dt} + Y_i \sum_{k=1}^K w_k W_k = (\omega_i + w_i) W_i \quad (1.2)$$

$$\rho_g \bar{C}_{pg} \frac{dT_g}{dt} + \sum_i h_i (w_i + \omega_i) W_i = N_p (Q_h + Q_{con,g}) \quad (1.3)$$

Additionally, the equation of state for perfect gas is:

$$P = \rho R T / \bar{W} \quad \text{with} \quad \bar{W} = \frac{1}{\sum_i Y_i / W_i} \quad (1.4)$$

In Eq. (1.1), ρ_g and m_g are the density and mass of all gas-phase species; w_i is the production rate of species i because of surface heterogeneous reactions; W_i is the molecular weight of species i . In Eq. (1.2), Y_i is the mass fraction of species i ; ω_i is the production rate of species i because of gas-phase reactions. In Eq. (1.3), T_g is the gas-phase temperature; h_i is the enthalpy of species i ; N_p is the particle number density; Q_h represents the enthalpy transferred from a particle to the bulk gases as a result of mass transfer because of surface reactions; and $Q_{con,g}$ is the convective heat transfer between a particle and the bulk gases. Detailed derivation of Eqs. (1.1)–(1.3) is listed in Appendix.

The convective heat transfer $Q_{con,g}$ between a particle and the gases is defined as

$$Q_{con,g} = -h A_p (T_g - T_p) \quad (1.5)$$

where h is the convective heat transfer coefficient, and A_p is the reactive surface area of a particle. The coefficient h can be expressed as [15]

$$h = \frac{Nu k_g}{d_p} \frac{B}{\exp(B) - 1}, \quad B = \frac{\dot{m}_p \bar{C}_{pg}}{\pi d_p N u k_g} \quad (1.6)$$

where d_p is the external diameter of particles, and Nu is the Nusselt number. In the present low Reynolds flow, a value of 2 was chosen for the Nusselt number.

The enthalpy transfer between one particle and the bulk gas, Q_h , can be expressed as

$$Q_h = \sum_i w_i h'_i \quad (1.7)$$

Note if the species i is the gaseous reactant of the heterogeneous reactions, the value of h'_i is determined using the gas phase

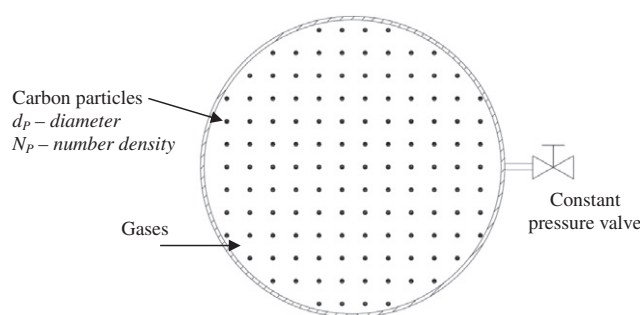


Fig. 1. Coal gasification in a well-stirred reactor.

temperature T_g . If the species i is the gaseous product of the heterogeneous reactions, the value of h'_i is determined using the particle temperature T_p .

A detailed gas-phase reaction mechanism, GRI-Mech 1.2, is incorporated into the model, which includes 177 elementary reactions and 31 species. The gas-phase species are H₂, H, O, O₂, OH, H₂O, HO₂, H₂O₂, C, CH, CH₂, CH₂(S), CH₃, CH₄, CO, CO₂, HCO, CH₂O, CH₂OH, CH₃O, CH₃OH, C₂H, C₂H₂, C₂H₃, C₂H₄, C₂H₅, C₂H₆, HCCO, CH₂CO, HCCOH, and N₂. Various transport properties and variable thermodynamic properties were adopted based on the CHEMKIN format. GRI-Mech 3.0 mechanism was also used, and the results are essentially the same as those of GRI-Mech 1.2.

2.2. Particle-phase equations

The particle mass m_p , density ρ_p , diameter d_p , number density N_p , and temperature T_p are the five variables to solve. The governing equations are:

$$\frac{dm_p}{dt} = \frac{\sum w_i W_i}{N_p} = \dot{m}_c \quad (2.1)$$

$$\rho_p = \rho_{p,0} \times \frac{m_p}{m_{p,0}} \quad (2.2)$$

$$d_p = d_{p,0} \quad (2.3)$$

$$N_p = N_{p,0} \frac{\rho_g}{m_g} \quad (2.4)$$

$$m_p C_{p,p} \frac{dT_p}{dt} = Q_{con,p} + Q_c - Q_{p,rad} \quad (2.5)$$

where $\rho_{p,0}$, $m_{p,0}$, $d_{p,0}$, and $N_{p,0}$ are the initial density, mass, diameter, and number density of each particle at $t = 0$ s. \dot{m}_c is the carbon consumption rate because of heterogeneous surface reactions; $C_{p,p}$ is the heat capacity of particles; $Q_{con,p}$ is the convective heat transfer between a particle and the bulk gases, expressed as $Q_{con,p} = hAp(T_g - T_p) = -Q_{con,g}$ (see Eq. (1.3)); and $Q_{p,rad}$ is the radiative heat transfer between a particle and the wall, which can be expressed as

$$Q_{p,rad} = \varepsilon \sigma \pi d_p^2 (T_w^4 - T_p^4) \quad (2.6)$$

where ε , σ and T_w are particle surface emissivity, Stefan–Boltzmann constant and the wall temperature, respectively. Previous studies have shown in gasifiers gas phase radiation are much less important than particle phase radiation. Thus here we neglected the radiative heat transfer between the hot gases and the wall, as well as the radiative heat transfer among particles which is a reasonable assumption for dilute to moderate particle number densities. To help understand Eqs. (2.1)–(2.6), the assumptions, models, and mechanisms used for carbon gasification are presented in the following. It is well known that the physical structure of a carbon or char particle changes during conversion as a result of surface reactions. Empirical correlations have been developed for particle diameter and density to describe the transformation. For example, the Carbon Burnout Kinetics (CBK), a kinetics package that describes char conversion developed by Sandia National Laboratories [16], assumed:

$$\frac{\rho}{\rho_0} = \left(\frac{m}{m_0}\right)^{\alpha}, \quad \frac{d_p}{d_{p,0}} = \left(\frac{\rho}{\rho_0}\right)^{-1/3} \left(\frac{m}{m_0}\right)^{1/3} \quad (2.7)$$

where subscript 0 denotes the initial value. The value of α is estimated to be between 0.95 and 1 for both entrained flow gasification and fluidized bed gasification [16]. In the present model, we used 1 for α , which results in a linear relationship between ρ and m , as shown by Eq. (2.2), and a constant external diameter d_p , as shown

by Eq. (2.3). Note Eq. (2.4) describes the change of particle number density as a result of change of volume under the assumption of constant pressure.

Furthermore, char surface area evolves during gasification, and usually results in a porous structure. The Random Pore Model [17,18] has been widely used to quantitatively describe the evolution. The present work adapted the Random Pore Model by imposing a factor f_{RPM} into the gasification rate [16]. This factor accounts for the pore surface evolution because of carbon conversion:

$$f_{RPM} = \sqrt{1 - \psi_0 \ln(1 - x)} \quad (2.8)$$

where x is the carbon conversion ratio; ψ_0 is a structural parameter, with an empirical value in a range of 2.2–7.7 [16] for most chars. Here, a mean value of 4.6 as suggested in Ref. [16] is used.

In Eq. (2.5), Q_c is the gross thermal energy released by all surface reactions, which can be written as

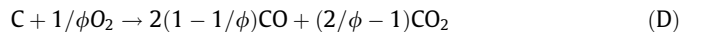
$$Q_c = \sum \dot{m}_{C,k} Q_{C,k} \quad (2.9)$$

$$\dot{m}_c = \sum \dot{m}_{C,k} \quad (2.10)$$

where $\dot{m}_{C,k}$ and $Q_{C,k}$ are the carbon consumption rate and the net heat of reaction of carbon surface reactions A, B, C, or D. Here we assume all heat from surface reactions is absorbed by particles because their thermal conductivity is much higher than that of the gases. These surface reactions and the rate constant as well as gas transport in the boundary layer are described in the following.

2.3. Carbon surface reactions

Four heterogeneous reactions are assumed to take place on the particle surfaces:



Reaction D is the carbon–oxygen reaction, which can produce both CO and CO₂. The ratio of CO to CO₂ depends on particle size and temperature. The empirical parameter ϕ in Reaction D is obtained following [4]:

$$\phi = \begin{cases} (2Z+2)/(Z+2) & \text{for } d_p \leq 0.005 \text{ cm} \\ [(2Z+2) - Z(d_p - 0.005)]/(Z+2) & \text{for } 0.005 \text{ cm} < d_p \leq 0.1 \text{ cm} \\ 1.0 & \text{for } d_p > 0.1 \text{ cm} \end{cases} \quad (3.1)$$

$$Z = 2500 \exp(-6249/T) \quad (3.2)$$

$$T = (T_p + T_g)/2 \quad (3.3)$$

The global rate of each reaction was simulated using the diffusion-kinetic model [19], which is of the first order for reactions A, B, and D, and of the second order for reaction C. The carbon reaction rate can be written as

$$\dot{m}_{C,k} = -A_p K_k (P X_{k,s})^n \quad (3.4)$$

where subscription k denotes reactions A, B, C, or D; K_k is surface reaction rate constant; $X_{k,s}$ is the mole fraction of the gaseous reactant at particle surface. The surface reaction rate constant is expressed in Arrhenius form as

$$K_k = B_k \exp\left(-\frac{E_k}{RT_p}\right) \quad (3.5)$$

where B_k is the prefactor; and E_k is the activation energy. The kinetic constant and the references from which they were obtained are listed in Table 1.

The transport rate of reactant gases to carbon surface was determined by bulk diffusion through an external boundary layer. Pore diffusion through an ash layer that could form over the char surface during later stages of gasification was neglected. The impact of the internal porous structure on the surface reaction rate was accounted by the Random Pore Model, as discussed in the previous section.

From the mass-based carbon reaction rate Eq. (3.4), the carbon molar reaction rate per unit area can be expressed as

$$\dot{n}_{C,k} = -K_k(PX_{k,s})^n/W_C \quad (3.6)$$

where W_C is the molecular weight of carbon. Then molar flux of gaseous species at the particle surface can be expressed as

$$\dot{n}_{H_2O} = \dot{n}_{CA} \quad (3.7.1)$$

$$\dot{n}_{CO_2} = \dot{n}_{CB} - (2/\phi - 1)\dot{n}_{CD} \quad (3.7.2)$$

$$\dot{n}_{H_2} = -\dot{n}_{CA} + 2\dot{n}_{CC} \quad (3.7.3)$$

$$\dot{n}_{CO} = -\dot{n}_{CA} - 2\dot{n}_{CB} - 2(1 - 1/\phi)\dot{n}_{CD} \quad (3.7.4)$$

$$\dot{n}_{O_2} = 1/\phi \dot{n}_{CD} \quad (3.7.5)$$

$$\dot{n}_{CH_4} = -\dot{n}_{CC} \quad (3.7.6)$$

The mole fraction of the reactant gases at particle surface is related to the molar flux and mass transfer coefficient by the following transport equations in the boundary layer that surrounds the particle as [20]

$$\dot{n}_i - X_{i,s} \sum \dot{n}_i = k_{im}(X_{i,\infty} - X_{i,s}) \quad (3.8)$$

where the subscripts s and ∞ denote particle surface and ambient; i is the gaseous species involved in the surface reactions; $X_{i,s}$ and $X_{i,\infty}$ are the mole fraction of species i on particle surface and in bulk, respectively; k_{im} is the mass transfer coefficient, which can be obtained from the Sherwood number correlation for spheres in a convective flow [20] as

$$Sh = \frac{k_{im}d_p}{C_s D_{im}} = 2 + 0.6Re^{1/2}Sc^{1/3} \approx 2 \quad (3.9)$$

where Sh is the Sherwood number, and a value of 2 was chosen for the present low Reynolds flow. C_s is the total gas concentration at the film at particle surface temperature, D_{im} is the molecular diffusivity of species i at the film temperature.

Given the mole fraction of H_2O , CO_2 , H_2 and O_2 in the gas phase, Eqs. (3.6)–(3.9) form a closed nonlinear system with the unknowns being the surface mole fraction of the gaseous reactants, $X_{i,s}$. The nonlinear equation system is solved using the DNEQNF solver in

Table 1
Reaction rate constants and heat of reaction.

Reaction	$k_s = B \exp(-A/T_p)$	$Q_C (10^7 \text{ erg/g})$
	B	A
A [29,30]	247	21,060
B [29,30]	247	21,060
C [10,30]	0.12	17,921
D [10,30]	8710	17,967
		$-2(1 - 1/\phi) \times 10,260 - 2(2/\phi - 1) \times 33,830^a$

^a ϕ is a parameter determined by particle diameter and the mean temperature of the particle and the gas.

the IMSL library [21]. The solver uses a modified Powell hybrid algorithm and a finite-difference approximation to the Jacobian. Once the surface mole fractions of these species are obtained, the consumption rates of carbon from each reaction can also be determined by Eq. (3.4).

2.4. Numerical method

The gas-phase and particle-phase governing equations, which form a closed ODE system, were solved using FORTRAN package DASPK3.1 [22]. DASPK was designed to solve large-scale Differential-Algebraic Equation (DAE) systems. After the initial condition for every variable and the convergence criteria were specified, DASPK integrated the equations over time. The time step size and the order of temporal discretization were dynamically determined by the solver itself.

3. Results and discussions

3.1. Model validation

To validate the model and the numerical code, we compared the simulation results with experimental data in the literature. Gregg et al. [23] conducted a series of experiments to gasify sub-bituminous coal, activated carbon, coke, and a mixture of coal and biomass in a 23 kW solar furnace. The sunlight coming through a reactor window was focused directly on the coal bed being gasified. Steam was passed through the solar-heated coal bed where it reacted with the coal and thus formed a combustible product gas. Among the many experimental coal gasification studies in literature, this experiment is most representative of the particle scale processes within the multi-scale reactor model developed in the present study.

The experimental data for validation used here are for gasification of activated carbon with steam. The composition of the activated carbon include 93.4% C, 0.6% H, 1.5% S, 0.2% ash, 0.2% acid-evolved CO_2 , and 0.2% moisture [23], which is close to the carbon used in the present work. The initial size of the carbon particles in the experiment was 5 mm and the reactor wall temperature was maintained around 1050 K. In the experiment, the energy used for gasification was provided through admission of estimated solar flux of $4.8 \times 10^5 \text{ W/m}^2$ through a large window. Other experimental conditions are listed in Table 2.

A comparison of the computed results and the experimental data for dry based concentrations of major species is shown in Fig. 2. The results show good agreement between the computed and the experimental data for major species. For comparison, results based on the calculations of Sane et al. [13], who assumed bulk gas-phase equilibrium for the water gas shift reaction, are also shown.

3.2. Typical gasification process without oxygen

Numerical simulations were conducted at various operating conditions (e.g., initial T , P , and reactant composition) to gain a fundamental understanding of the gasification processes and to identify the most influential parameters for gasification performance, including carbon conversion time, syngas production and composition, and CO_2 emission. We first considered a basic case for which no oxygen was initially present in the reactant mixture. To provide the heat needed for the endothermic surface reactions, a constant wall temperature of 1100 K was assumed. The reactor is filled with uniformly distributed carbon particles and steam, both at a temperature of 1200 K and a pressure of 10 atm. The initial H_2O/C ratio is 2, the particle size is 100 μm , and the initial and final particle

Table 2

Initial conditions for the validating case.

Initial gas temperature	$T_g = 1050\text{ K}$	Initial particle temperature	$T_p = 1050\text{ K}$
Wall temperature	$T_w = 755\text{ K}$	Solar energy density	$J = 4.8 \times 10^5\text{ W/m}^2$
Gas pressure	$P = 1\text{ atm}$	Density of particles	$\rho_p = 0.9\text{ g/cm}^3$
Initial water concentration	$X_{H_2O} = 1.0$	Initial particle diameter	$d_p = 5\text{ mm}$
Initial H ₂ O/C molar ratio	H ₂ O/C = 3.0		

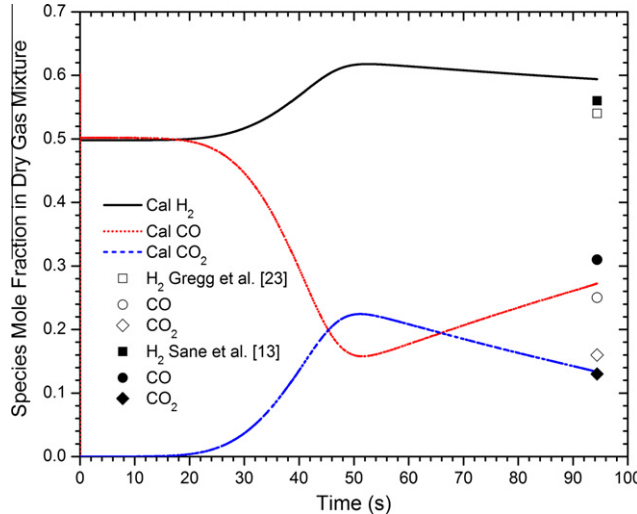


Fig. 2. Profiles of the computed and measured species concentrations as a function of time. Experimental data are from Ref. [23].

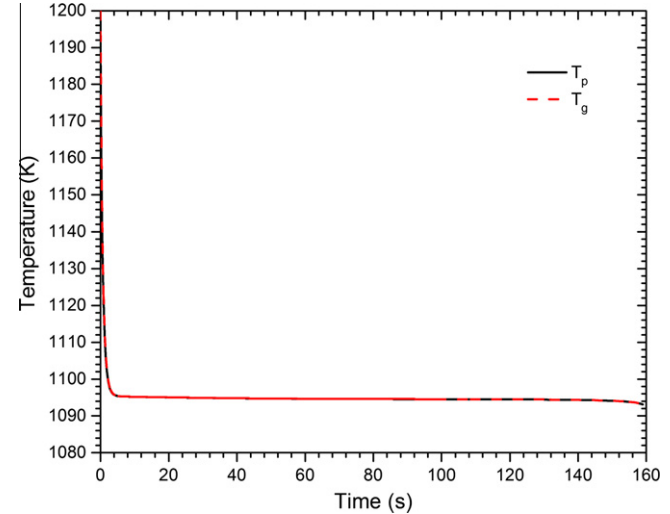


Fig. 3. Profiles of the gas and particle temperatures as functions of time for the basic case without O₂. Initial conditions are listed in Table 3.

Table 3

Initial conditions for a typical gasification process without oxygen.

Initial gas temperature	$T_g = 1200\text{ K}$	Initial particle temperature	$T_p = 1200\text{ K}$
Wall temperature	$T_w = 1100\text{ K}$	Density of particles	$\rho_p = 1.3\text{ g/cm}^3$
Gas pressure	$P = 10\text{ atm}$	Initial particle diameter	$d_p = 100\text{ }\mu\text{m}$
Initial water concentration	$X_{H_2O} = 1.0$	Particle number density	$N_p = 896/\text{cm}^3$
Initial H ₂ O/C molar ratio	H ₂ O/C = 2.0		

number density is 896/cm³. These representative parameters used in the present simulation are listed in Table 3.

Figure 3 shows the temperature profiles of T_p and T_g as a function of time. The particle and the gas have nearly the same temperatures during the gasification process. Both temperatures decrease to 1095 K at $t = 4\text{ s}$, from 1200 K at $t = 0\text{ s}$. The decrease in temperature is because of the endothermic nature of the surface reactions ($\text{C} + \text{H}_2\text{O} = \text{CO} + \text{H}_2$ and $\text{C} + \text{CO}_2 = 2\text{CO}$). After $t = 4\text{ s}$, the temperatures remain almost constant.

To understand energy conversion during the gasification process, we compared the source terms in the gas-phase energy equations, which include the total heat produced by the gas-phase reactions, convective heat transfer, and enthalpy transfer because of the mass transfer resulting from the surface reactions, respectively. These terms plotted as functions of time, are shown in Fig. 4. In the first four seconds, these terms change rapidly. Especially, the convective heat transfer shows a negative spike. In the later stage ($t > 4\text{ s}$), the terms remain almost constant. The convective heat transfer is nearly zero because the difference between T_p and T_g is negligible.

Furthermore, we examined the energy balance of the 177 detailed elementary reactions and identified five that have the high-

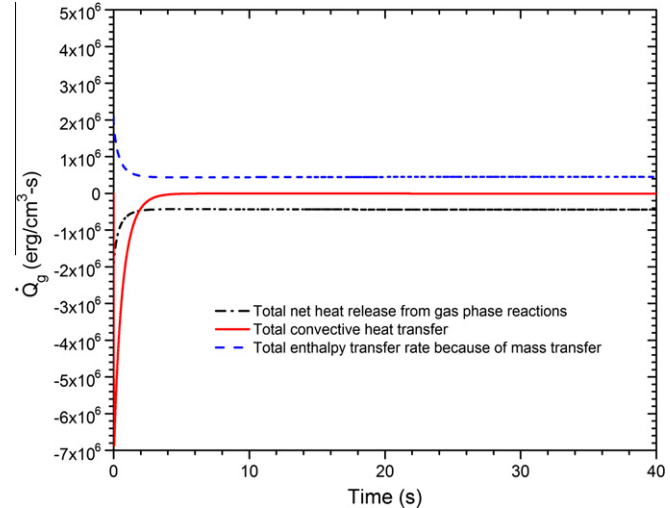


Fig. 4. Comparison of the source terms in the gas-phase energy equation for the basic case without O₂. Initial conditions are listed in Table 3.

est energy release, as shown in Fig. 5. These reactions are $\text{OH} + \text{H}_2 = \text{H} + \text{H}_2\text{O}$, $\text{OH} + \text{CH}_4 = \text{CH}_3 + \text{H}_2\text{O}$, $\text{H} + \text{CH}_4 = \text{CH}_3 + \text{H}_2$, $\text{OH} + \text{CH}_2\text{O} = \text{HCO} + \text{H}_2\text{O}$, and $\text{H} + \text{CH}_2\text{O} = \text{HCO} + \text{H}_2$. Among them, the energy release from $\text{OH} + \text{H}_2 = \text{H} + \text{H}_2\text{O}$ reaction is a few magnitudes larger than that from the others, indicating that it is the most influential elementary reaction in the gas phase. The energy release rates change in the first 40 s and remain almost constant at a later stage of the gasification process.

Figure 6 shows the concentration profiles of five stable species including H₂, H₂O, CO, CO₂, and CH₄. The carbon conversion rate as functions of time is also shown. The overall conversion time is about 160 s. Note that the simulation ends when 99% of the carbon

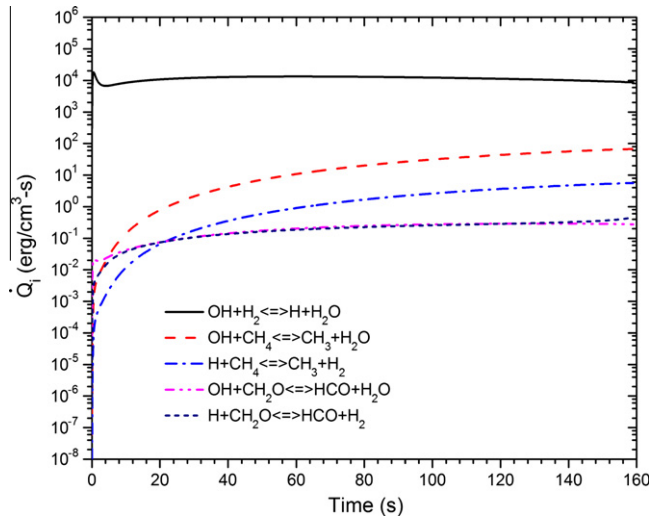


Fig. 5. Profiles of the heat release rate as a function of time of five main gas-phase elementary reactions for the basic case without O_2 . Initial conditions are listed in Table 3.

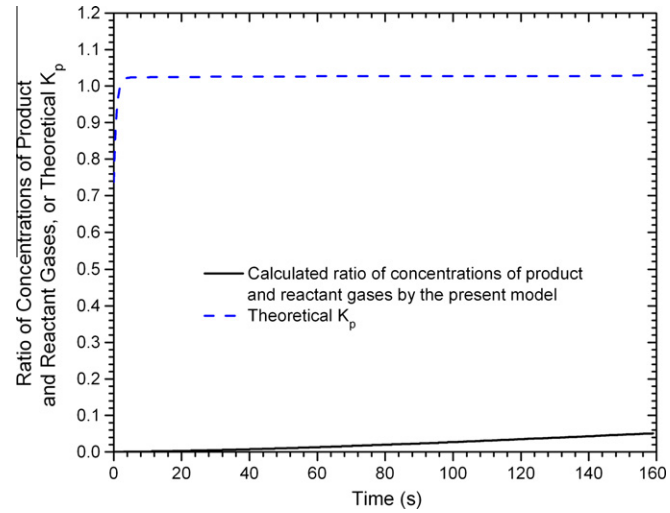


Fig. 7. Computed ratio of concentrations of product and reactant gases and theoretical equilibrium constant of water-gas-shift reaction as a function of time for the basic case without O_2 . Computed ratios of concentrations are based on detailed chemistry calculations; theoretical K_p are calculated using the polynomial expression in Ref. [24]. Initial conditions are listed in Table 3.

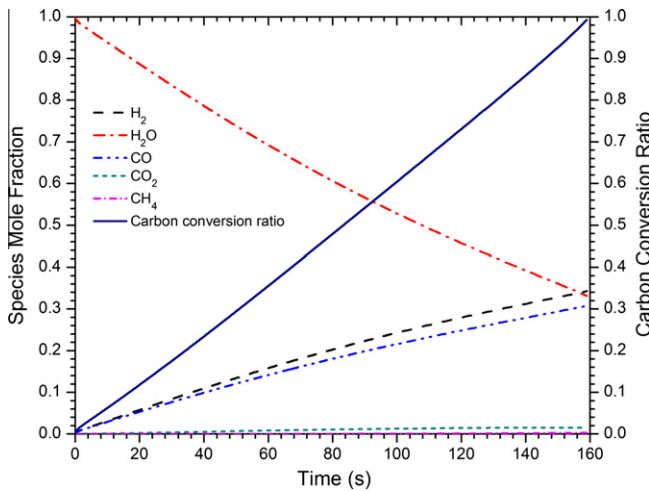


Fig. 6. Profiles of species concentrations and carbon conversion rate as functions of time for the basic case without O_2 . Initial conditions are listed in Table 3.

particles are gasified. The concentrations of intermediate and minor species are not shown, which are much lower than those of the stable species. At the end of the gasification process, 34.3% H_2 , 30.8% CO , and 1.5% CO_2 are produced in the wet gas mixture.

The water-gas-shift reaction ($\text{CO} + \text{H}_2\text{O} = \text{CO}_2 + \text{H}_2$) is often assumed to be at equilibrium in most modeling studies. To evaluate this assumption, we calculated the ratio $= X_{\text{CO}_2}X_{\text{H}_2}/(X_{\text{CO}}X_{\text{H}_2\text{O}})$ by using the simulation results (in equilibrium this ratio is equal to the equilibrium constant K_p), where the concentrations of H_2O , CO , H_2 , and CO_2 are obtained from the present detailed-chemistry calculations. Figure 7 shows the ratio $= X_{\text{CO}_2}X_{\text{H}_2}/(X_{\text{CO}}X_{\text{H}_2\text{O}})$ as a function of time. The concentration ratio is compared to the equilibrium constant obtained using the an empirical expression from Ref. [24]. The K_p has a polynomial dependence on temperature expressed as: $\ln(K_p) = -3.49 + 3.563 * (10^3/T_g) + 0.313 * (10^3/T_g)^2$. The expression was obtained by nonlinear regression based on the data in the JANAF Thermochemical Table [25], and the accuracy of the resulting value of K_p is better than 1%. The comparison of Fig. 7 clearly shows that the ratio of concentrations is not equal to the K_p value over the entire time, indicating that the water-gas-shift

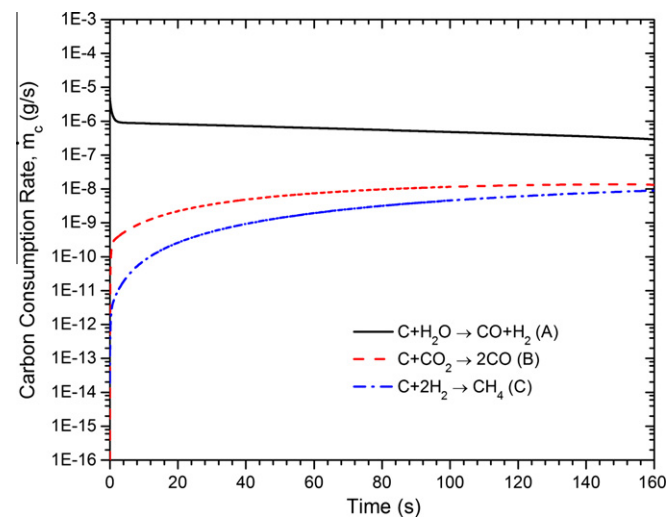


Fig. 8. Profiles of carbon consumption rates of three surface reactions as functions of time for the basic case without O_2 . Initial conditions are listed in Table 3.

reaction is not in equilibrium. The reason for the nonequilibrium might be the extreme temperature sensitivity of the elemental reactions at the relatively low temperatures (below 1200 K), as suggested by Gregg et al. [26]. This extreme sensitivity to temperature in the relatively low temperature range is similar to the extreme sensitivity to temperature in the ignition regime of combustion processes. The results, point to a need for future experimental and theoretical investigations of the threshold gasification temperature.

A better understanding of the relative importance of the three surface reactions is reached when we view in Fig. 8 the rates of reactions A, B, and C, based on a single particle plotted as functions of time. The absolute values of the reaction rates decrease rapidly soon after the gasification reactions start. Later the absolute values of the reaction rates retain almost constant very low values bearing resemblance to analogous extinction regime in combustion processes. The rate of $\text{C} + \text{H}_2\text{O} \rightarrow \text{CO} + \text{H}_2$ reaction is much faster than the rates of $\text{C} + \text{CO}_2 \rightarrow 2\text{CO}$ and $\text{C} + 2\text{H}_2 \rightarrow \text{CH}_4$ reactions. However,

all three rates are significantly slower than those during the initial transient.

Figure 9 shows the source terms in the particle-phase energy equation, based on a representative single particle out of the 895 identically gasifying particles per cm^3 in the reactor, including heat release from reactions A, B, and C, as well as convective heat transfer between the two phases and the radiation heat transfer between the single particle and the wall in the presence of an isotropic mixture of identical participating particles. Because of the endothermic nature of the three surface reactions, the particle temperature and the gas temperature both decrease after the reactions start. Of the three surface reactions, reaction A ($\text{C} + \text{H}_2\text{O} \rightarrow \text{CO} + \text{H}_2$) consumes the most energy. Moreover, the radiation energy exchanged between the particle and the wall is significant at the later stages of the gasification process. Depending on the wall temperature, the radiation exchange may provide the energy needed for the endothermic surface reactions and prevent ceasing of gasification observed in the present example.

3.3. Typical gasification process in the presence of oxygen

Because the carbon-steam reaction absorbs energy, practical gasifiers need to be heated to maintain a high-temperature environment so that the gasification reactions can proceed. The heat sources can be electric, partial oxidation of coal (combustion of coal), or oxidation of an auxiliary fuel such as natural gas in the gasifier. Partial oxidation of coal using externally injected oxygen is a more common practice because it is cost-effective. We emulated partial oxidation of coal by including a small amount of oxygen in the initial mixture. The carbon-oxygen reactions during the initial stage are to be designed to provide sufficient energy to the system. Similar to the previous example, we assume an adiabatic process and use identical initial temperature, pressure, particle diameter, and $\text{H}_2\text{O}/\text{C}$ molar ratio. The only difference is that the reactant mixture now contains 20% O_2 and the wall temperature T_w is 500 K. The initial conditions are summarized in Table 4.

Figure 10 shows the temperature profiles of T_p and T_g as a function of time. The particle and gas temperatures increase rapidly to a maximum ($T_p = 1850$ K and $T_g = 2460$ K). During the initial period, T_p is higher than T_g ($t < 0.02$ s), but it becomes lower during the rest of the gasification process. The peak temperatures occur at the instant of complete oxygen depletion, as can be seen in Fig. 11, which also shows the concentration profiles of the six main stable gaseous species as a function of time.

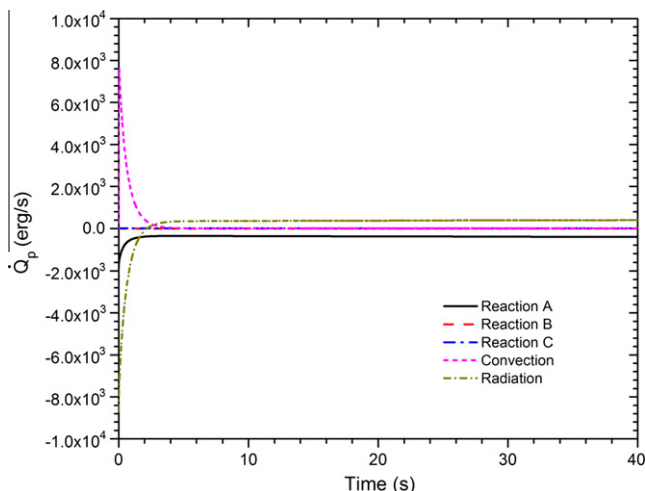


Fig. 9. Comparison of the source terms in the particle-phase energy equation for the basic case without O_2 . Initial conditions are listed in Table 3.

Also shown in Fig. 11 is the carbon conversion rate as a function of time. The gasification process needs about 0.1 s to be complete. During the interval, $0 \text{ s} < t < 0.015 \text{ s}$, CO concentration first increases slightly, then decreases to zero. During the interval, $0 \text{ s} < t < 0.034 \text{ s}$, oxygen concentration approaches negligible levels, while CO_2 concentration increases to a maximum (18%). During this period, the carbon surface oxidation reaction ($\text{C} + 1/\phi\text{O}_2 \rightarrow 2(1 - 1/\phi)\text{CO} + (2/\phi - 1)\text{CO}_2$) and the gas-phase reactions are dominant and consume most of the oxygen. For $t > 0.034 \text{ s}$ when O_2 is consumed and the peak temperature has been achieved, carbon surface reactions A, B, and C become more important. Especially the carbon-steam reaction A, which causes the concentrations of CO and H_2 to increase and the concentration of H_2O to decrease, and the surface reaction B which reduces CO_2 while removing a C atom from the carbon surface to produce two molecules of CO are important.

In the initial period, oxidation reactions of both the bulk gas phase and the particle surface and gas phase occur. Gas-phase oxidation reactions mainly include the elementary steps $\text{OH} + \text{CO} = \text{H} + \text{CO}_2$, $\text{H} + \text{O}_2 + \text{H}_2\text{O} = \text{HO}_2 + \text{H}_2\text{O}$, $\text{OH} + \text{HO}_2 = \text{O}_2 + \text{H}_2\text{O}$, $\text{H} + \text{O}_2 = \text{O} + \text{OH}$, $\text{OH} + \text{H}_2 = \text{H} + \text{H}_2\text{O}$, $2\text{OH} = \text{O} + \text{H}_2\text{O}$ and $2\text{OH} + \text{M} = \text{H}_2\text{O}_2 + \text{M}$. The reaction rates of these seven steps are plotted as functions of time in Fig. 12. The rates of the gas-phase reactions are much faster than those of the solid-gas reactions. The gas-phase oxidation reactions are dominant in the presence of O_2 . The gas-phase temperature T_g reaches a peak value that is higher than the peak particle-phase temperature T_p because of the large energy release rate of the gas-phase oxidation reactions. Later in the gasification process, after the oxygen is completely consumed, T_p and T_g both begin to decrease because of the endothermic nature of the surface reactions.

Figure 13 shows the reaction rates of reactions A, B, C, and D as functions of time. During the initial period, the rate of $\text{C} + 1/\phi\text{O}_2 \rightarrow 2(1 - 1/\phi)\text{CO} + (2/\phi - 1)\text{CO}_2$ reaction is much higher (100 times) than the rate of $\text{C} + \text{H}_2\text{O} \rightarrow \text{CO} + \text{H}_2$ reaction. After the oxygen is depleted, the carbon-steam reaction becomes dominant, with a rate about 10 or more times higher than the rates of $\text{C} + \text{CO}_2 \rightarrow 2\text{CO}$ and the $\text{C} + 2\text{H}_2 \rightarrow \text{CH}_4$ reactions. Based on Figs. 10–13, one can divide the gasification process into three stages: (1) carbon oxidation, (2) gas-phase oxidation, and (3) carbon gasification, as noted in Figs. 10–13.

The carbon oxidation reaction D can be considered as a combination of two reactions, $2\text{C} + \text{O}_2 \rightarrow 2\text{CO}$ and $\text{C} + \text{O}_2 \rightarrow \text{CO}_2$. To find the relative importance of these two reactions, the ratio of $2(1 - 1/\phi)/(2/\phi - 1)$ is plotted as a function of time in Fig. 14. It shows that the ratio of CO to CO_2 changes in the range of 9.5–28. This means that the concentration of CO_2 is much less than CO and the $\text{C} + \text{O}_2 \rightarrow \text{CO}_2$ reaction could be neglected for high temperature carbon oxidation.

Char porosity plays an important role in gasification, and is a key factor that impacts reaction rates. In the present simulations, a random pore model [17,18] was used to count for the pore surface evolution as well as its impact on the gasification rates. Figure 15 shows the profile of the factor f_{RPM} as a function of time. Note f_{RPM} represents the ratio of the internal surface area of the pores to the constant outer surface area of the particle. This factor was imposed into the gasification rate to account for the increase of internal surface area during carbon conversion. Figure 15 shows the factor gradually increases with time. At the end of the gasification process, this factor reaches a value of 5.6, indicating that the pore structure does play an essential role in enhancing the reaction rates and the gasification process.

The particle and the gas phases have not only energy transfer, but also mass transfer resulting from the surface reactions that consume and produce gaseous species. This alters the gas-phase composition by the diffusion process. Figure 16 shows the net

Table 4

Initial conditions for a typical gasification process with presence of oxygen.

Initial gas temperature	$T_g = 1200 \text{ K}$	Initial particle temperature	$T_p = 1200 \text{ K}$
Wall temperature	$T_w = 500 \text{ K}$	Density of particles	$\rho_p = 1.3 \text{ g/cm}^3$
Gas pressure	$P = 10 \text{ atm}$	Initial particle diameter	$d_p = 100 \mu\text{m}$
Initial water concentration	$X_{H_2O} = 0.8$	Initial oxygen concentration	$X_{O_2} = 0.2$
Initial H ₂ O/C molar ratio	$H_2O/C = 2.0$	Particle number density	$N_p = 828/\text{cm}^3$

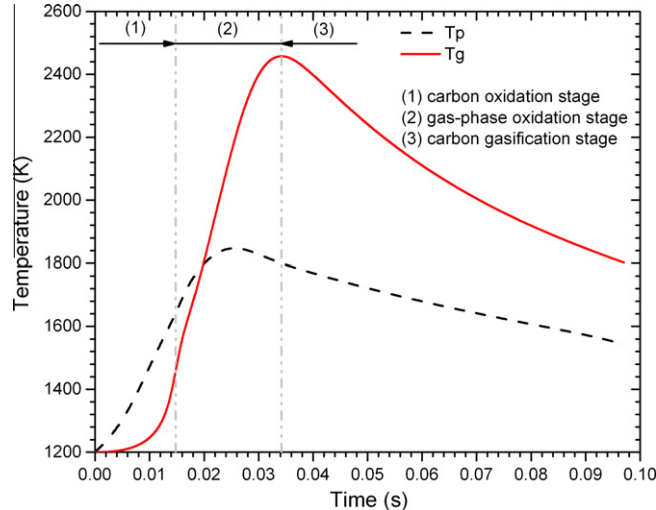


Fig. 10. Profiles of gas and particle temperature as functions of time for the basic case with O₂. Initial conditions are listed in Table 4.

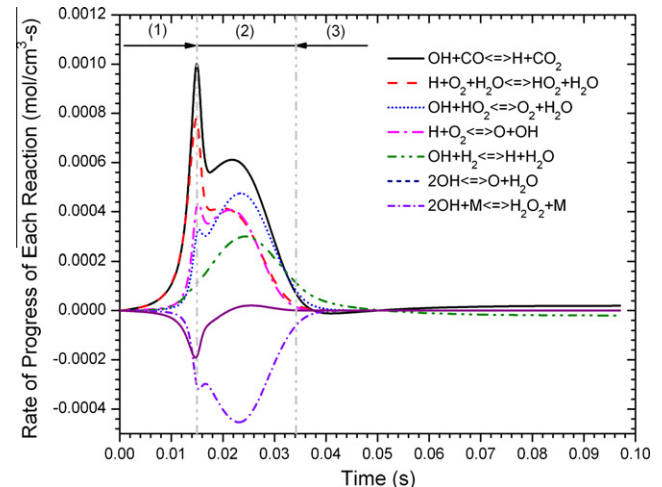


Fig. 12. Profiles of rate of progress of main gas-phase elementary reactions for the basic case with O₂. Initial conditions are listed in Table 4.

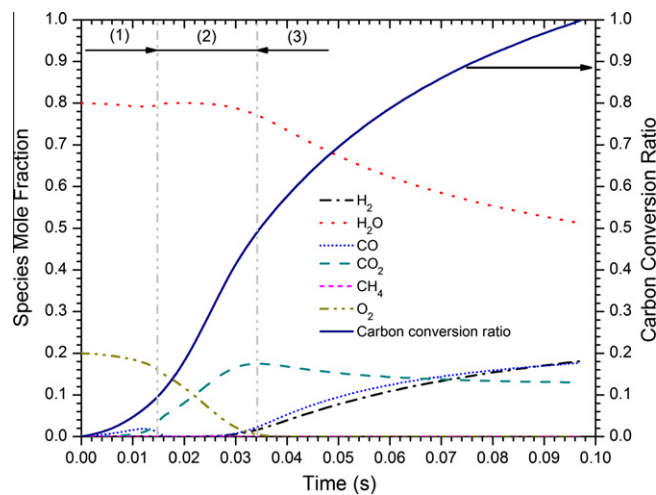


Fig. 11. Profiles of species concentration and carbon conversion rate as functions of time for the basic case with O₂. Initial conditions are listed in Table 4.

production rates of five stable species as functions of time. The CO production rate from surface reactions is determined by reactions $2C + O_2 \rightarrow 2CO$, $C + O_2 \rightarrow CO_2$, $C + H_2O \rightarrow CO + H_2$, and $C + CO_2 \rightarrow 2CO$, especially the first three reactions. This explains the fact that the CO concentration versus time curve has a peak at $t = 0.025 \text{ s}$, which is between the peak of the O₂ curve ($t = 0.022 \text{ s}$) and the peak of the H₂O curve ($t = 0.028 \text{ s}$). CO₂ is first produced from the carbon oxidation reaction and then is consumed in reaction $C + CO_2 \rightarrow 2CO$ in gas-phase oxidation stage and carbon gasification stage.

As discussed earlier, the gas temperature changes because of heat release from gas-phase reactions, energy transfer because of the mass transfer from particle surface reactions, as well as convective

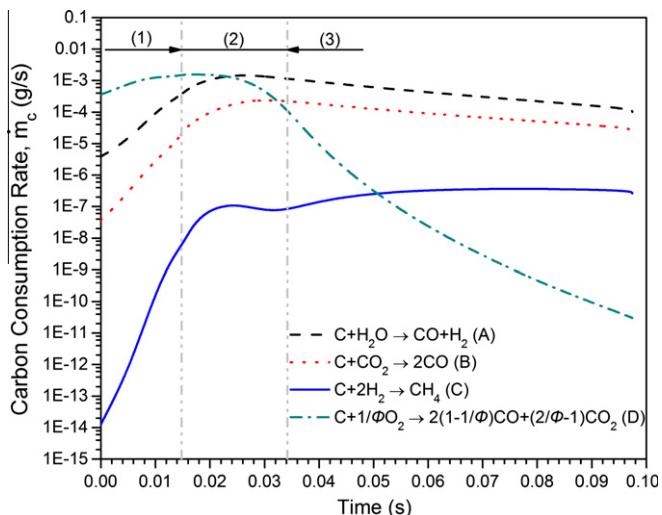


Fig. 13. Profiles of carbon consumption rates of four surface reactions as functions of time for the basic case with O₂. Initial conditions are listed in Table 4.

heat transfer between the two phases. The particle temperature changes because of heat release/absorption from surface heterogeneous reactions, convective heat transfer and radiation. The source terms in the gas and particle-phase energy equations are discussed below to improve our understanding of the energy coupling between the two phases and to identify the most influential parameters in the gasification process.

Figure 17 shows the source terms in the particle energy equation, including heat release from reactions A, B, C, and D, the convective heat transfer between the two phases and radiation between a particle and the wall. As shown in Fig. 17, the heat released by reaction D (the carbon oxidation reaction) and the

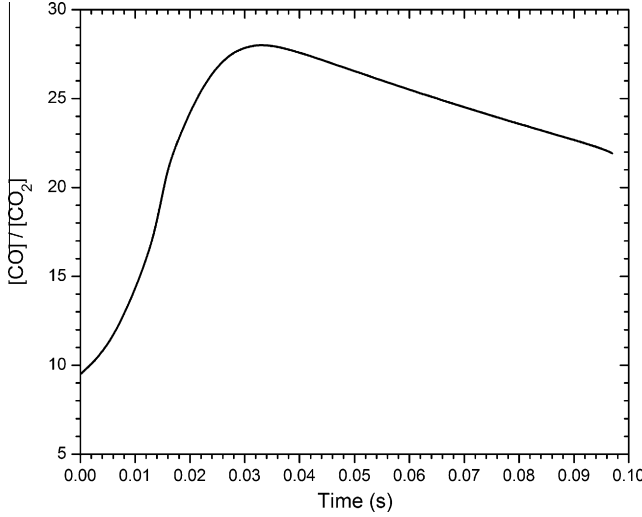


Fig. 14. The ratio of CO to CO_2 in reaction D as a function of time for the basic case with O_2 . Initial conditions are listed in Table 4.

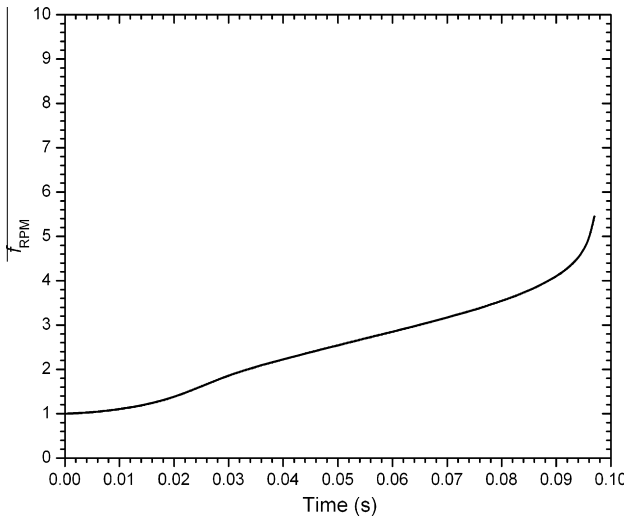


Fig. 15. Profile of f_{RPM} as a function of time for the basic case with O_2 . f_{RPM} is the ratio of the internal surface area of the pores to the constant outer surface area of the particle. Initial conditions are listed in Table 4.

convective heat transfer between a particle and surrounding gases are most important in the initial stages. The former increases the particle temperature, and the latter increases the gas temperature by convection. The energy absorbed by reaction A ($\text{C} + \text{H}_2\text{O} \rightarrow \text{CO} + \text{H}_2$) and the convective heat transfer from the gas phase to the solid surface are more important post- O_2 consumption in comparison to the heat absorbed by the reactions A, B ($\text{C} + \text{CO}_2 \rightarrow 2\text{CO}$) and C ($\text{C} + 2\text{H}_2 \rightarrow \text{CH}_4$). The effects of radiation heat transfer decline as the particle surface and gas phase temperatures are reduced by the post- O_2 endothermic processes.

Figure 18 shows a comparison of three source terms in the gas phase energy equation, including the total heat generated by the gas-phase reactions, convective heat transfer, and enthalpy transfer because of mass transfer from the surface reactions. In the initial stages, the total energy released by the gas-phase reactions is dominant. A peak of the sensible energy generated by the gas-phase reactions occurs around $t = 0.015$ s. Later during the gasification stage, the three source terms change very little.

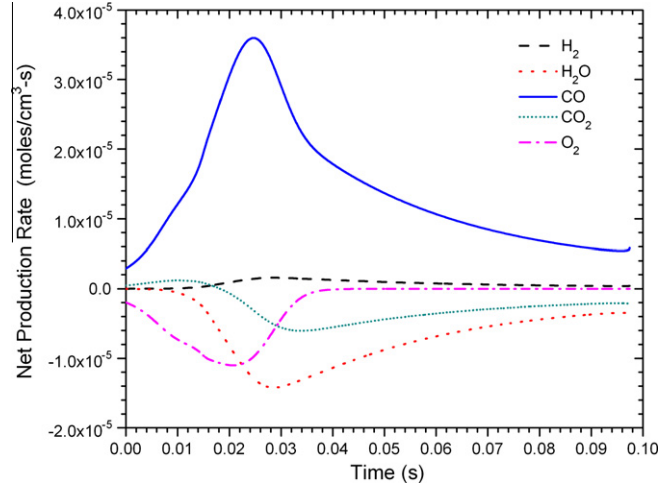


Fig. 16. Net production rate of five species resulting from surface heterogeneous reactions for the basic case with O_2 . Initial conditions are listed in Table 4.

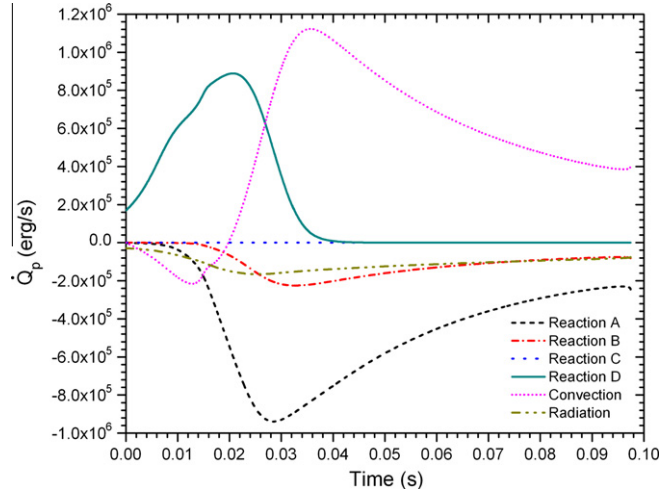


Fig. 17. Comparison of the source terms in the particle-phase energy equation for the basic case with O_2 . Initial conditions are listed in Table 4.

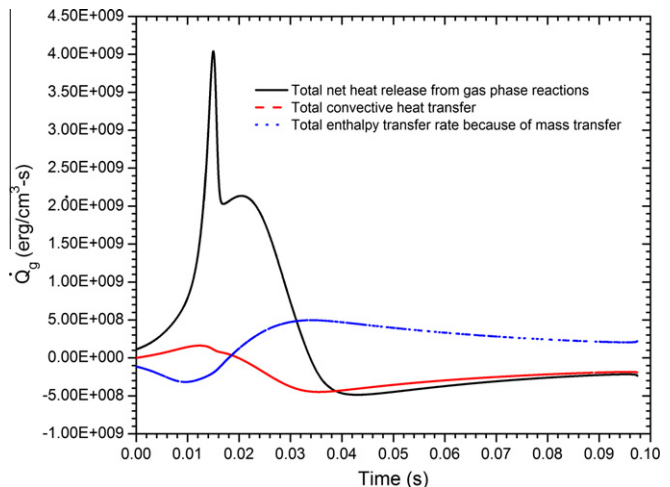


Fig. 18. Comparison of source terms in the gas-phase energy equation for the basic case with O_2 . Initial conditions are listed in Table 4.

Lastly, we evaluated the assumption of the water-gas-shift reaction to be at equilibrium. The ratio representing the multiplication of product concentrations divided by the multiplication of the reactant concentrations of the water gas shift reaction (product of the concentrations of H_2O and CO divided by the product of the concentrations of CO_2 , and H_2) obtained from the detailed chemistry calculations was compared to theoretical equilibrium constant. The results are shown in Fig. 19. It can be seen that the values have reasonable agreement in the later phases of the gasification process, indicating that the water-gas-shift reaction is at least near equilibrium state. This was not observed for the low temperature gasification case discussed earlier in the paper and depicted in Fig. 7. This is consistent with previous studies that suggested that at high temperatures the water-gas-shift reaction can be assumed to be at equilibrium [24,27].

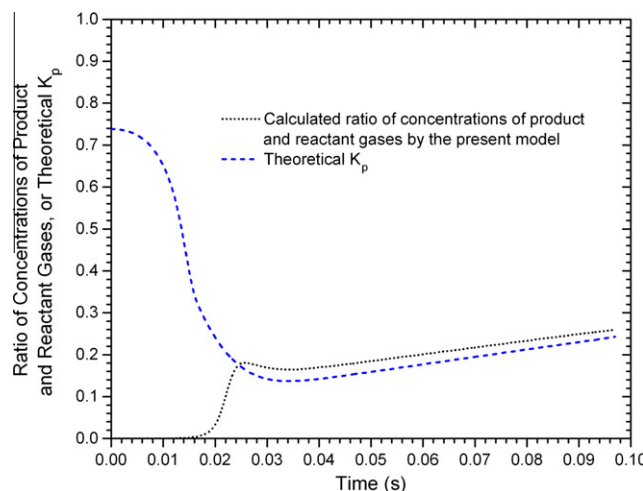


Fig. 19. Computed ratio of concentrations of product and reactant gases and theoretical equilibrium constant of water-gas-shift reaction as a function of time for the basic case with O_2 . The ratio of concentrations of product and reactant gases are based on detailed chemistry calculations; theoretical K_p are calculated using the polynomial expression in Ref. [24]. Initial conditions are listed in Table 4.

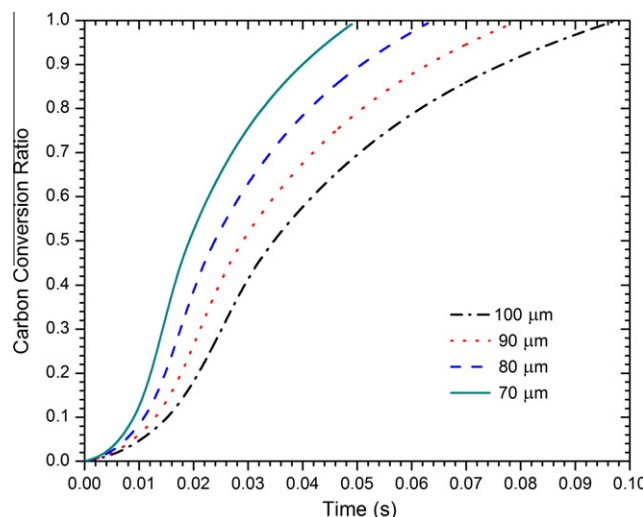


Fig. 20. Carbon conversion ratio as functions of time for $d_p = 100 \mu m$, $90 \mu m$, $80 \mu m$, and $70 \mu m$ for the basic case with O_2 . Other initial conditions are listed in Table 4.

3.4. Effect of particle size

Parametric studies were conducted to understand the effects of process conditions on the gasification processes. First, the effect of particle size on carbon conversion rate was examined. Figure 20 compares the total conversion time of four mixtures containing carbon particles of various sizes in the range $70\text{--}100 \mu m$. Note we kept the carbon mass the same for all four mixtures, which means the particle-number densities are different but still within the independent particle regime. Other initial conditions were the same as discussed in Session 3.3 (see Table 4). The results show that as expected the carbon conversion time is significantly reduced with a decrease of particle size. The reason can be seen from Figs. 21 and 22, which compare the profiles of the gas and particle temperature (Fig. 21) and the carbon consumption rate (Fig. 22) for $d_p = 100 \mu m$ and $70 \mu m$, respectively. Figure 21 shows that for smaller particles, T_p and T_g reach their peak values more rapidly. This means the heat transfer by means of conduction and convection is more effective in raising the temperature of smaller particles. The resulting rapid surface reaction rates lead to shorter

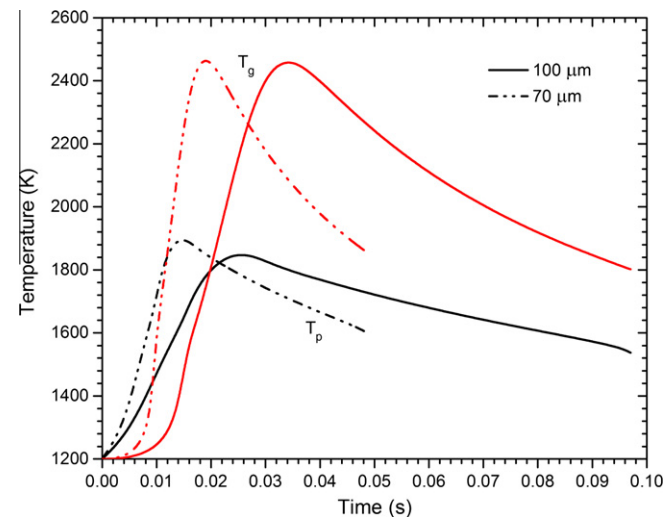


Fig. 21. Profiles of gas and particle temperature for $d_p = 100 \mu m$ and $70 \mu m$ for the basic case with O_2 . Other initial conditions are listed in Table 4.

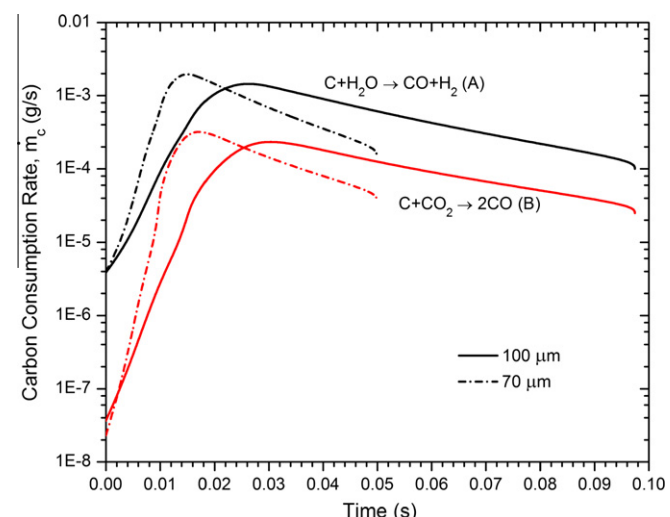


Fig. 22. Carbon consumption rate for $d_p = 100 \mu m$ and $70 \mu m$ for the basic case with O_2 . Other initial conditions are listed in Table 4.

conversion times as shown in Fig. 22. Lastly, particle size has no impact on the final CO_2 emission.

3.5. Effect of radiation

Radiative heat transfer can be a strong energy transport mechanism in real gasifiers. Radiation heat loss from particles can be significant at high temperatures. In the following, we will discuss the effect of radiative heat transfer between the particles and the wall on the gasification process using an example discussed in Section 3.3 (the basic case with O_2 , see Table 4). Note the wall temperature was assumed to be 500 K. Figure 23 compares the temperature profiles calculated with and without consideration of radiation. It can be seen the peak T_p and T_g are about 50 K lower when radiation is included. The difference, however, is small at later stages when T_p and T_g both decrease. Because of the lower temperatures resulting from radiation heat loss, the reaction rates are lower. As a result, the carbon conversion time is longer: the total conversion times are 0.075 s (without radiation heat loss) and 0.097 s (with radiation heat loss).

3.6. Effect of pressure

Simulations were conducted for the same reactant mixture at various pressures to understand the effect of pressure on the gasification process and the carbon conversion rate. Figure 24 shows the carbon conversion ratio as a function of time at pressures of 10, 12, 14, and 16 atm, respectively. Other initial conditions are listed in Table 4. The differences in the carbon conversion time (0.05 s at 16 atm vs. 0.097 s at 10 atm) indicate that pressure has a significant influence on the gasification process. Figure 25 shows a comparison of the reaction rates of the two surface reactions at 10 atm and 14 atm. It can be seen that the peak rates at 14 atm are several times larger than those at 10 atm, thus reducing the overall time required for gasification. This is because the reaction rate constant is proportional to the pressure. Also, the species mole fractions at the particle surface are higher at high pressures, leading to corresponding increases in the surface reaction rates.

3.7. Effect of oxygen concentration

Simulations were conducted for reactant mixtures containing various concentrations of O_2 based on the example discussed

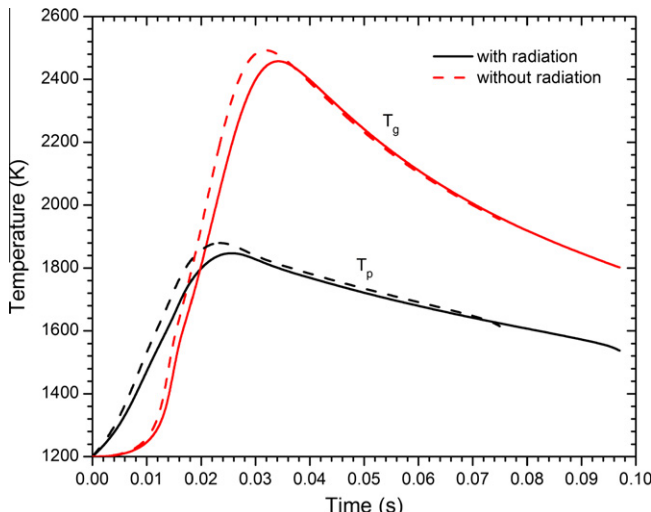


Fig. 23. Profiles of gas and particle temperature for the case with radiation and without radiation for the basic case with O_2 . Initial conditions are listed in Table 4.

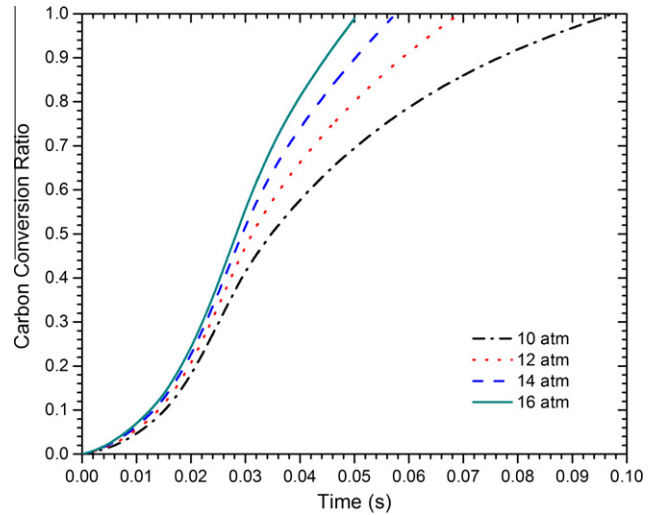


Fig. 24. Carbon conversion ratio as functions of time for 10 atm, 12 atm, 14 atm, and 16 atm for the basic case with O_2 . Other initial conditions are listed in Table 4.

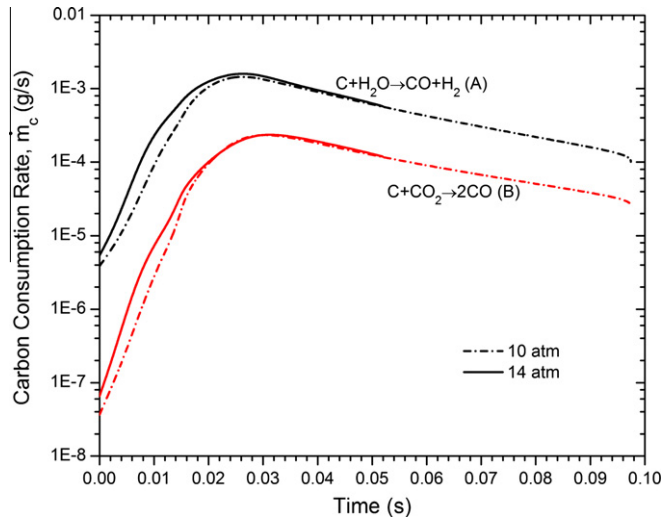


Fig. 25. Carbon consumption rate of two surface heterogeneous reactions as functions of time for 10 atm and 14 atm for the basic case with O_2 . Other initial conditions are listed in Table 4.

in Session C. Figure 26 depicts the carbon conversion rates as functions of time for various O_2 concentrations. The results show that the O_2 concentration affects carbon conversion times significantly (0.153 s at $X_{\text{O}_2} = 18\%$ vs. 0.057 s at $X_{\text{O}_2} = 24\%$). At higher O_2 concentrations, O_2 is depleted faster. The heat released by the exothermic oxidation reactions results in higher particle and gas temperatures, which consequently and subsequently increase the carbon conversion rate. During the gasification process, the peak CO_2 concentration increases with increasing O_2 concentration. However, by the end of the gasification process, the final CO_2 concentration remains almost the same for all four cases.

3.8. Effect of hydrogen addition

Coal gasification technology is being explored as a means to produce liquid fuels for the transportation sector. However, the gasification process also releases CO_2 , which can be a concern. Agrawal et al. [28] proposed a hybrid hydrogen-carbon (H2CAR) process for the production of liquid fuels, in which there is no

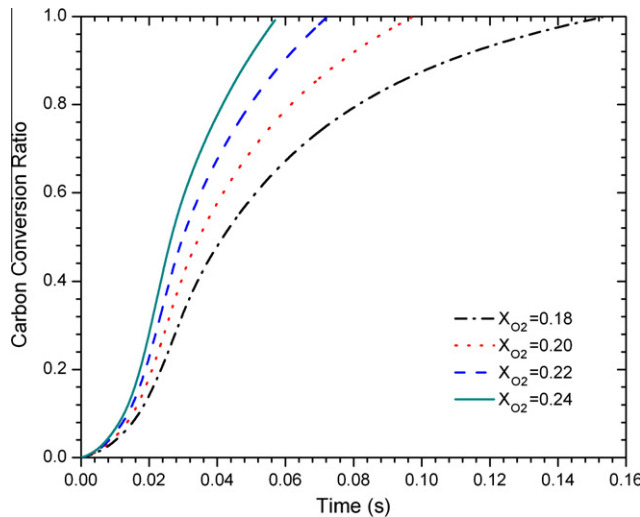


Fig. 26. Carbon conversion ratios as functions of time for $X_{O_2} = 0.18$, $X_{O_2} = 0.20$, $X_{O_2} = 0.22$, and $X_{O_2} = 0.24$ for the basic case with O₂. Other initial conditions are listed in Table 4.

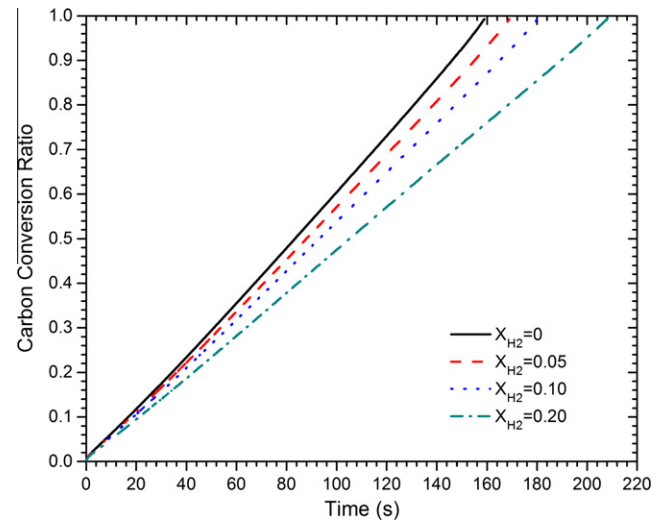


Fig. 27. Carbon conversion ratio as functions of time for $X_{H_2} = 0$, $X_{H_2} = 0.05$, $X_{H_2} = 0.10$, and $X_{H_2} = 0.20$ for the basic case with O₂. Other initial conditions are listed in Table 4.

CO₂ emission from the chemical processing system. In this proposal, coal or biomass is used to provide carbon atoms needed for the production of liquid hydrocarbons, and hydrogen, generated from carbon-free primary energy sources such as solar, nuclear, and wind, is used to supply the hydrogen atoms needed for the chemical transformation. The authors proposed feeding H₂ from a carbon-free energy source and recycling CO₂ back to the gasifier, which could potentially minimize the net CO₂ formation by promoting the reverse water-gas-shift reaction.

Motivated by this proposal, we conducted simulations to investigate the effects of H₂ addition on carbon conversion and CO₂ emission. Here we used the example discussed in Section 3.2, and the initial conditions are listed in Table 3. Following Sane et al. [13], H₂ was added in two ways: one of the ways involved addition of H₂ in the initial reactant mixture, which is called bulk addition. The second way is defined as linear addition, involving continuous H₂ addition at a constant rate after a certain amount of carbon has been consumed. For the purpose of comparison, the total amount of hydrogen added to the system was maintained identical for the two methods. And for the latter, H₂ was added linearly after 70% carbon had been consumed.

Figures 27 and 28 respectively show the carbon conversion ratio and CO₂ concentration as a function of time for H₂ addition at 0%, 5%, 10%, and 20%, when the bulk addition method is used. The results show that increasing the hydrogen concentration increases the overall conversion time. For example, with 20% H₂ addition in the initial reactant mixture, the conversion time increases to 209 s, from 159 s with 0% H₂ addition. This is because a fast diffusion of H₂ to the surface of the particles reduces the concentration of H₂O at that location, thus reducing the surface reaction rate of the coal-steam reaction. The results in Fig. 28 show that increasing the H₂ concentration in the initial reactant mixture decreases CO₂ concentration. This verifies the hypothesis that the addition of H₂ can reduce CO₂ emission, driving the equilibrium of the water-gas-shift reaction away from CO₂.

Figures 29 and 30 respectively show the concentration profiles of six stable species and the carbon conversion rate using the bulk addition and the linear addition method. The total amount of hydrogen added to the reactor is the same for both methods, 20%. However, the conversion time is shorter in the linear addition method, ~162 s vs. ~209 s. As discussed above, the carbon consumption rate is mainly determined by the rates of surface reac-

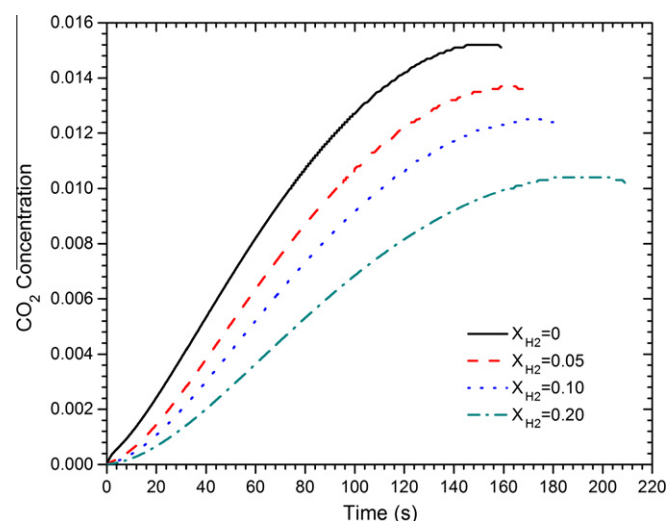


Fig. 28. CO₂ concentration as functions of time for $X_{H_2} = 0$, $X_{H_2} = 0.05$, $X_{H_2} = 0.10$, and $X_{H_2} = 0.20$ for the basic case with O₂. Other initial conditions are listed in Table 4.

tions C + O₂ → CO and C + H₂O → CO + H₂, which are largely affected by the concentration of O₂ and H₂O on particle surface through boundary layer diffusion. In the H₂ bulk addition method, because of the high diffusivity of H₂, the concentration of O₂ and H₂O at the surface of the carbon particle was reduced, which decreased the total carbon consumption rate. In the linear addition method, however, H₂ was progressively added when 70% carbon had been consumed; thus it only affected the later stages of particle gasification. Lastly, by comparing Figs. 29, 30 and 11, we find that both methods of H₂ addition can increase syngas production (CO and H₂) and decrease CO₂ emissions by shifting the water gas reaction.

4. Summary and conclusions

A multiphysics model with detailed gas-phase chemistry was developed for the first time to simulate the complex gasification processes in a well-stirred reactor. The use of multistep detailed

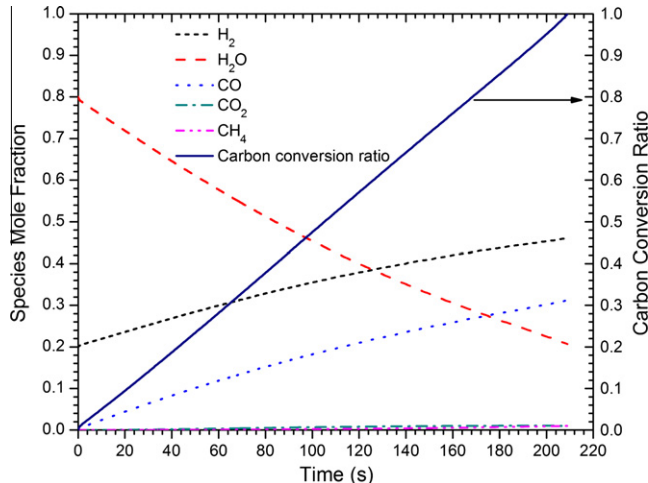


Fig. 29. Profiles of species concentration and carbon conversion rate as functions of time for the H₂ bulk addition method. H₂ ($X_{H_2} = 0.20$) was added one time to the initial reactant mixture. Other initial conditions are listed in Table 3.

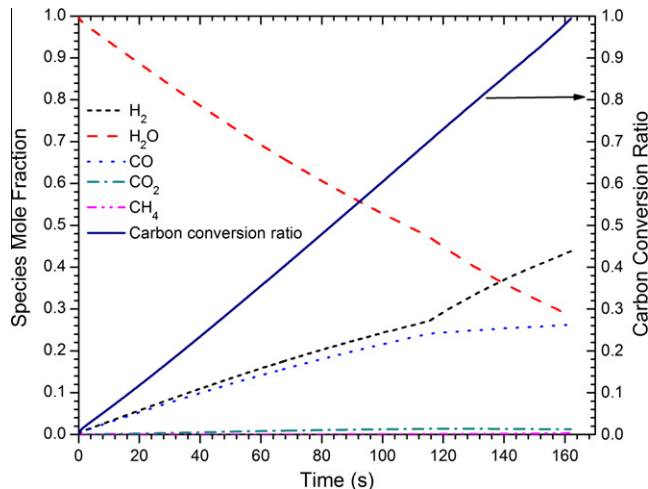


Fig. 30. Profiles of species concentration and carbon conversion rate as functions of time for the H₂ linear addition method. The same total amount of H₂ as the bulk addition method was added continuously at a constant rate after 70% of carbon had been consumed. Other initial conditions are listed in Table 3.

chemistry and variable thermodynamic and transport properties represents a specific improvement over the bulk scale gas-phase equilibrium assumed by Sane et al. [13]. The model considers detailed gas-phase and particle-phase reactions, radiative heat transfer, as well as full coupling (mass, species, and energy exchanges) between the two phases at various scales. The evolution of char porous structure and its effect on the gasification rate was modeled by a random pore model. The present numerical simulations lead to the following major conclusions:

In the pure gasification process when no O₂ is presented in the initial reactant mixture, the particle temperature and the gas temperature both decrease because of the endothermic nature of the surface reactions. The amount of the convective heat transfer between particles and the surrounding gases is dominant, reducing the difference between the particle and the gas temperatures to relatively small values.

With the presence of oxygen in the reactant mixture, the chemical process in the reactor can be divided into three stages: (1) carbon oxidation, (2) gas-phase oxidation, and (3) carbon gasification. In the first two stages, the exothermic oxidation reactions domi-

nate, which release heat and provide a high-temperature environment. This supports the endothermic surface reactions that become dominant in the later stage. In the first stage, the reaction rate of $2C + O_2 \rightarrow 2CO$ is much faster than the other surface reactions. In the later stages, $C + H_2O \rightarrow CO + H_2$ reaction dominates the consumption of carbon at a rate much faster than those of $C + CO_2 \rightarrow 2CO$ and $C + 2H_2 \rightarrow CH_4$.

The water-gas-shift reaction was found to be nearly in equilibrium for relatively high temperatures. However, at low temperatures the water-gas shift does not reach an equilibrium state because the rates of all reactions are relatively low.

The total carbon conversion time increases with increasing particle size. This is because the heat by means of conduction and convection can raise the temperature of smaller particles more rapidly, thus increasing the surface reaction rates and reducing the conversion time.

Increasing pressure results in shorter carbon conversion times because of increased surface reaction rates. Carbon conversion is also sensitive to O₂ concentration. An increase in O₂ concentration increases the particle and gas temperatures and thus reduces the carbon conversion time. Additionally, radiation heat losses from the particles to the wall decrease both the particle and gas temperatures, increasing the conversion time.

The addition of H₂ can reduce CO₂ emission by driving the equilibrium of the water-gas-shift reaction toward CO and H₂O. But it also reduces the carbon conversion rate because the H₂O concentration on particle surface is reduced by the fast diffusion of H₂. The linear addition method results in shorter carbon conversion times than the bulk addition method.

Acknowledgments

This work was supported by the Air Force Office of Scientific Research under the technical management of Dr. Julian Tishkoff. Support from the Purdue Energy Fund is also appreciated.

Appendix A

A.1. Derivation of the gas phase conservation equations

The continuity equation, the species conservation equation, and the energy conservation equation for a system with volume V , a pressure P , and mass/energy transfer between the gas phase and particle phase are given as

$$\frac{d(\rho_g V)}{dt} = V \sum w_i W_i \quad (A1)$$

$$\frac{d(\rho_g V Y_i)}{dt} = V (\omega_i + w_i) W_i \quad (A2)$$

$$\frac{d(\rho_g V e)}{dt} = V N_p (Q_h + Q_{con,g}) - P \frac{dV}{dt} \quad (A3)$$

where ρ_g is the total density of gas-phase species; w_i is the production rate of species i because of surface heterogeneous reactions; W_i is the molecular weight of species i . In Eq. (A2), Y_i is the mass fraction of species i ; ω_i is the production rate of species i because of gas-phase reactions. In Eq. (A3), e is the internal energy of the bulk gases; N_p is the particle number density; Q_h represents the enthalpy transferred from a particle to the bulk gases as a result of mass transfer because of surface reactions; and $Q_{con,g}$ is the convective heat transfer between a particle and the bulk gases.

The ideal gas equation of state and the constant pressure equation are also included.

$$\rho_g = P \bar{W} / R T_g \quad (A4)$$

$$\frac{dP}{dt} = 0 \quad (\text{A5})$$

where $\bar{W} = \sum_i \frac{Y_i}{W_i}$, R is the gas constant, and T_g is the gas-phase temperature.

Since $m_g = \rho_g V$, replacing $\rho_g V$ with m_g in Eqs. (A1)–(A3) yields

$$\frac{1}{m_g} \frac{dm_g}{dt} = \frac{1}{\rho_g} \sum w_i W_i \quad (\text{A6})$$

$$\frac{d(m_g Y_i)}{dt} = \frac{m_g}{\rho_g} (\omega_i + w_i) W_i \quad (\text{A7})$$

$$\frac{d(m_g e)}{dt} = \frac{m_g}{\rho_g} N_p (Q_h + Q_{con,g}) - P \frac{dV}{dt} \quad (\text{A8})$$

where $\sum w_i W_i = \dot{m}_c N_p$, and $\dot{m}_c = \sum \dot{m}_{c,k}$ (see Eq. (2.10)).

Using Eq. (A6), the species conservation Eq. (A7) becomes

$$\rho_g \frac{dY_i}{dt} + Y_i \sum_{k=1}^K w_k W_k - (\omega_i + w_i) W_i = 0 \quad (\text{A9})$$

With the definition of the internal energy, the left hand side of the energy Eq. (A8) becomes

$$\frac{d(m_g e)}{dt} = \frac{d(m_g (h - P/\rho_g))}{dt} = \frac{d(m_g h - VP)}{dt} = \frac{dm_g h}{dt} - \frac{dPV}{dt} \quad (\text{A10})$$

The first term on the right-hand of Eq. (A10) can be expressed as

$$\begin{aligned} \frac{dm_g h}{dt} &= \frac{dm_g \sum_i h_i Y_i}{dt} = \sum_i \frac{dm_g h_i Y_i}{dt} \\ &= \sum_i h_i \frac{dm_g Y_i}{dt} + \sum_i m_g Y_i \frac{dh_i}{dt} \\ &= \frac{m_g}{\rho} \sum_i h_i (\omega_i + \omega_i) W_i + m_g \bar{C}_{p,g} \frac{dT_g}{dt} \end{aligned} \quad (\text{A11})$$

where $\bar{C}_{p,g}$ is the mean specific heat capacity of the mixture.

Combining Eqs. (A8), (A10), and (A11), the energy equation becomes

$$\begin{aligned} \frac{m_g}{\rho} \sum_i h_i (\omega_i + \omega_i) W_i + m_g \bar{C}_{p,g} \frac{dT_g}{dt} \\ = \frac{m_g}{\rho_g} N_p (Q_h + Q_{con,g}) + V \frac{dP}{dt} \end{aligned} \quad (\text{A12})$$

With constant pressure assumption (Eq. (A5)), the energy equation is

$$\rho_g \bar{C}_{p,g} \frac{dT_g}{dt} + \sum_i h_i (\omega_i + \omega_i) W_i = N_p (Q_h + Q_{con,g}) \quad (\text{A13})$$

In summary, the continuity equation, the species conservation equation, and the energy conservation equation can be expressed as Eqs. (A6), (A9), and (A13).

References

- [1] B. Srinivas, N.R. Amundson, AIChE J. 26 (3) (1980) 487–496.
- [2] H.W. Haynes, AIChE J. 28 (3) (1982) 517–521.
- [3] E.V. Samoilov, M.F. Faminskaya, E.S. Golovina, Combust. Explos. Shock Waves 40 (1) (2004) 77–84.
- [4] R. Govind, J. Shah, AIChE J. 30 (1) (1984) 79–92.
- [5] Q.H. Ni, A. Williams, Fuel 74 (1) (1995) 102–110.
- [6] D. Vamvuka, E.T. Woodburn, P.R. Senior, Fuel 74 (10) (1995) 1452–1460.
- [7] G.S. Liu et al., Fuel 79 (14) (2000) 1767–1779.
- [8] C.X. Chen, M. Horio, T. Kojima, Chem. Eng. Sci. 55 (18) (2000) 3861–3874.
- [9] D.F. Fletcher et al., Appl. Math. Model. 24 (3) (2000) 165–182.
- [10] X.J. Liu, W.R. Zhang, T.J. Park, Combust. Theor. Model. 5 (4) (2001) 595–608.
- [11] W. Vicente et al., Appl. Therm. Eng. 23 (15) (2003) 1993–2008.
- [12] Y.X. Wu et al., Energy Fuels 24 (2010) 1170–1175.
- [13] A. Sane, Y. Zheng, J. Gore, A Study of Steam Gasification of Coal with CO₂ Control using H₂, in: The 6th US National Combustion Meeting, Ann Arbor, Michigan, May 2009.
- [14] M. Frenklach, H.W., C.-L. Yu, M. Goldenberg, C.T. Bowman, R.K. Hanson, D.F. Davidson, E.J. Chang, G.P. Smith, D.M. Golden, W.C. Gardiner, V. Lissianski, Gas Research Institute Topical Report: M. Frenklach, H. Wang, M. Goldenberg, G.P. Smith, D.M. Golden, C.T. Bowman, R.K. Hanson, W.C. Gardiner and V. Lissianski, 'GRI-Mech—An Optimized Detailed Chemical Reaction Mechanism for Methane Combustion,' Report No. GRI-95/0058, November 1, 1995, Gas Research Institute <http://www.me.berkeley.edu/gri_mech/>.
- [15] Y.C. Guo, C.K. Chan, K.S. Lau, Fuel 82 (8) (2003) 893–907.
- [16] G.S. Liu, S. Niksa, Prog. Energy Combust. Sci. 30 (6) (2004) 679–717.
- [17] S.K. Bhatia, D.D. Perlmutter, AIChE J. 26 (3) (1980) 379–386.
- [18] S.K. Bhatia, D.D. Perlmutter, AIChE J. 27 (2) (1981) 247–254.
- [19] Zhou LX. Theory and Numerical Modeling of Turbulent Gas-Particle Flows and Combustion. Science Press, Beijing and CRC Press, Florida, 1993.
- [20] R.B. Bird, W.R. Stewart, E.N. Lightfoot, Transport Phenomena, John Wiley and Sons, New York, 1960.
- [21] Visual Numerics, I. IMSL Math/Library Online User's Guide Volume 1, <<http://www.vni.com>>.
- [22] L.R. Petzold, A description of DASSL: a differential/algebraic system solver, in: R.S. Stepleman et al. (Eds.), Scientific Computing, North-Holland, Amsterdam, 1983, pp. 65–68.
- [23] D.W. Gregg et al., Sol. Energy 25 (1980) 353–364.
- [24] J.L. Figueiredo, J.A. Moulijn, Sci. Affairs Div. (1986) 560–568.
- [25] D.R. Stull, H. Prophet, Janaf Thermochemical Tables vol. NSRDS–NBS 37, 1971, US Government Printing Office, Washington DC.
- [26] D.W. Gregg et al., Sol. Energy 24 (1979) 313–321.
- [27] A. David, Bell, B.F. Towler, Coal Gasification and Its Applications, Elsevier Inc. (2011) 138–139.
- [28] R. Agrawal et al., PNAS 104 (2007) 4828–4833.
- [29] J.L. Johnson, Kinetics of coal gasification (1979).
- [30] S. Dobner, Modelling of Entrained Bed Gasification: The Issues, in EPRI. 1976: Palo Alto, CA.